Available online at www.sciencedirect.com

ScienceDirect

Procedia Structural Integrity 53 (2024) 212–220

Structural Integrity Procedia

www.elsevier.com/locate/procedia

Third European Conference on the Structural Integrity of Additively Manufactures Materials (ESIAM23)

Cavitation erosion resistance of 1.2709 alloy produced via Laser-Powder Bed Fusion

Luca Marchini[a]*; Pietro Tonolini[a]; Lorenzo Montesano[a]; Marialaura Tocci[a]; Annalisa Pola[a]; Marcello Gelfi[a]

[a]*University of Brescia, Department of Mechanical and Industrial Engineering, Via Branze 38, Brescia 25123, Italy*

Abstract

Maraging steels, like 1.2709 (18Ni-300), are attractive materials for the aerospace, automotive, tooling, and bearing gear industries because of their high yield, tensile strength, and good toughness. The low-carbon martensite matrix and nanoscale intermetallic precipitates combine to provide distinctive mechanical properties. In particular, due to their low carbon content, these steels are easily weldable and are therefore appropriate for additive manufacturing (AM) processes like laser-based powder bed fusion (LPBF). The tooling and molding industry has just lately started using this fabrication technique to create inserts with conformal cooling channels that can extend the lifetime of the insert and core while boosting the cast quality. These parts are frequently exposed to high levels of stress, wear, and even aggressive conditions. In this context, this research focuses on a peculiar, and thus understudied, erosion phenomenon known as cavitation erosion. According to the ASTM G32 standard, the cavitation erosion resistance of 1.2709 maraging steel samples produced by additive manufacturing as well as by forging was investigated. Microstructural analyses were carried out to evaluate the effect of the different microstructures resulting from the different manufacturing techniques on erosion behavior. When compared to the forged maraging steel, the AM one shows less resistance to the initiation of the erosion phenomenon. Nevertheless, the wear rates of the two materials are comparable.

Keywords: Maraging steel; Cavitation erosion; L-PBF.

* Corresponding author. Tel.: +39 0303715826.
E-mail address: Luca.Marchini@unibs.it

10.1016/j.prostr.2024.01.026

1. Introduction

In high-temperature applications, achieving rapid and uniform heat regulation within a component is of paramount importance. To control heat flow effectively, conformal cooling channels (CCCs) have gained widespread use in automotive and aerospace components. Furthermore, the integration of CCCs within mold inserts is increasingly prevalent in both plastic injection molding (PIM) and high-pressure die-casting (HPDC) processes. CCCs excel in maximizing heat extraction where conventional cooling systems often fall short, thereby enhancing process performance and the final quality of components (Venkatesh *et al.*, 2017). Mold thermoregulation is essential for producing high-quality parts as well as improving the die life and production cycle, which have a significant impact on the process' cost-effectiveness.

In the context of HPDC, these inserts are becoming fundamental for meeting the demands of modern lightweight automotive structural castings with a low carbon footprint, whose production requires larger and more intricate dies (Yang *et al.*, 2023). The fabrication of CCCs has been greatly simplified, thanks to significant advancements in additive manufacturing (AM) technologies. Complex geometries, tailored for cooling applications, can now be seamlessly produced using AM techniques (Brooks and Brigden, 2016). Particularly, laser-based AM methods, such as laser powder bed fusion (L-PBF), are commonly employed for manufacturing CCCs with intricate designs (Peças *et al.*, 2019).

Within this scenario, maraging steels emerge as a solution that can address both the challenges associated with mold inserts and the characteristics of the L-PBF process. In fact, maraging steels offer a unique blend of high ultimate tensile strength (UTS) even at high temperature, exceptional fracture toughness, good weldability, and dimensional stability (Piekło and Garbacz-Klempka, 2020). These two latter properties result fundamental for the processability by L-PBF where the powder material is melted and welded, undergoing extremely rapid cooling rate. Thus, these properties have led to the adoption of maraging steels, such as 1.2709, as mold inserts, even though they exhibit lower heat conductivity compared to traditional mold tool steels (e.g., H11). However, this limitation could become negligible with the implementation of CCCs.

While the mechanical properties required for the intended applications of these components are well-documented, there exists a notable gap in our understanding of the surface properties of additively manufactured (AMed) maraging components, despite their critical importance in various applications. Surface quality is particularly crucial in mold areas where it can influence performance significantly. Notably, cavitation erosion stands out as a prominent mechanism responsible for surface damage when a component interacts with a liquid experiencing rapid pressure fluctuations (Abdullah *et al.*, 2011).

2. Materials and methods

The maraging steels under examination were produced by Deutsche Edelstahlwerke Specialty Steel GmbH & Co. KG by using two distinct manufacturing techniques. The first manufacturing process encompassed several steps, including electric arc furnace melting, ladle furnace refinement, vacuum arc remelting, and final forging (named process F).

For the AM samples, a commercial powder known as Printdur® Powderfort, with a composition close to 1.2709 maraging steel was employed (named process AM). Regarding the particle size of the AM feedstock material, approximately 3.4 vol.% of the particles has a diameter smaller than 20 µm, 45.6 vol.% smaller than 38 µm, and a significant 98.2 vol.% smaller than 53 µm. The powder exhibits a flow rate of 15.6 s/50g and has an apparent density of 3.99 g/cm^3. The fabrication of maraging steel samples through AM was accomplished using a commercially available laser-based powder bed fusion system which specific process parameters are classified information, as previously mentioned in the literature (Tonolini *et al.*, 2022). The resulting AM samples were discs, measuring 57 mm in diameter and 12 mm in height, with their axis oriented parallel to the building direction (BD).

In contrast, the forged maraging steel samples were derived from the Cryodur®2709 commercial alloy. These samples originated from a forged round bar with a diameter of 60 mm and were machined to match the sizes of the AM samples.

Table 1 shows the chemical composition of the AM and F maraging steels. The light difference in the percentage of alloying elements is related to the different manufacturing process requirements.

Table 1 - Samples mean chemical composition.

El. (wt%)	C	Si	Mn	P	S	Cr	Mo	Ni	Co	Ti	N	O	Fe
AM	0.01	0.2	0.3	0.01	0.006	0.1	5	17.9	13.4	-	0.007	0.026	Bal.
F	0.004	0.02	0.03	<0.003	0.0014	0.1	4.95	18.3	9.75	1.13	-	-	Bal.

Moreover, to attain comparable ultimate mechanical properties, notwithstanding the different manufacturing procedures, the specimens underwent distinct heat treatment processes. For the forged samples, this involved a one-hour solution treatment at 820 °C, followed by rapid cooling at room temperature in air, and final aging for 5 hours and 30 minutes at 490 °C. Conversely, for the AM samples, only an aging treatment was implemented. This process consisted of holding the samples at 490 °C for 4 hours, promoting the formation of precipitates, following the methodology outlined by (Casati *et al.*, 2016). Notably, these specific heat treatment parameters were chosen based on the manufacturer's expertise to achieve equivalent hardness levels for both the AM and F samples.

Optical analyses were performed by Leica DMI 5000M (Wetzalr, Germany) optical microscope (OM). The metallographic analysis was performed by etching the mirror polished samples with modified Fry's reagent and Nital 4%. Samples porosities were characterized in terms of fraction of area through the analysis of 10 images (magnification 500x) by OM. The fraction of porosities (%) was determined as the ratio between the total area of porosities and the analysed area of samples.

HRC hardness measurements were performed using an LTF Galileo Ergotest Comp 25 testing machine (applied load of 1471 N) on the investigated samples.

Cavitation tests were conducted following the "stationary specimen method", according to the ASTM G32-16 (2021) standard. The polished to mirror finish surface was exposed to cavitation. A Felisari GV2000 ultrasonic device with a vibration frequency of 20.0 kHz, a vibration amplitude of 50 μm, and a peak electrical power of 2 kW was utilized in the tests. The ultrasound probe (sonotrode) is composed of a Ti6Al4V waveguide and an Inconel 625 horn with a final amplification diameter of 18 mm (Girelli *et al.*, 2018). The sample was obtained by cutting with a metallographic saw starting from the discs and was brought, by polishing, to a dimension such that it could be inserted into a specially designed sample holder. Due to the shape of the starting samples, the surface perpendicular to the BD was the one exposed to testing. The test was carried out with the sample immersed in a tank containing distilled water, at a distance of 0.50 mm from the surface of the tip of the sonotrode at the rest position. The positioning was achieved using a tab with a thickness equal to the previously indicated distance, ensuring that the sample was securely held by the gripping system. The ambient temperature was maintained at 23 ± 2°C. Periodic interruptions of the test were made to measure the weight loss, with a precision of 0.1 mg, and observe the morphology of the eroded surface using a DMS300 digital microscope. The total test duration was set at 24 hours, upper time limit defined by the ASTM G32-16 standard, due to the high material resistance to erosion measured at early testing times.

The data were initially expressed as mean depth of erosion (MDE) and mean depth of erosion rate (MDER), as required by the standard. Additionally, for clarity, the results are presented in terms of cumulative mass loss over the test duration. Given the nearly identical densities of the materials, this presentation method was considered more suitable for the purpose of this study. For the calculation of MDE and MDER, the volume removed was determined based on the sample's density, while the surface of the material involved in the erosion was approximated as equal to the circular section of the tip of the sonotrode.

Low magnification images, obtained through a DSM300 digital microscope (Leica, Wetzlar, Germany), were used to analyse the erosion damage during the above reported steps. The displayed images are the result of digital merging of 9 shots per sample. In addition, cross sections of the samples at the end of the test were analysed by OM after polishing to mirror finish.

Finally, scanning electron microscope (LEO EVO 40, Carl Zeiss AG, Milan, Italy) was used for the analysis of the damaged surface after three selected test-time intervals (2, 4 and 8 hours).

3. Results and discussion

Fig. 1 presents optical microscope images, offering a representative view of the sections tested in the samples. Fig. 1a displays the microstructure of the forged samples after solution and aging treatment. When subjected to etching with Fry's reagent, a fully martensitic microstructure is revealed, characterized by martensite blocks with varying orientations. Fig. 1b showcases the surface of the additive manufactured sample. This surface is marked by cellular martensite, along with the recognizable overlapped and elongated scan tracks typically associated with as-built AM components. Importantly, after the aging treatment, the scan tracks remain observable. Additionally, the porosity detection from image analysis resulted in a 99.82 ± 0.08 % dense component. Whereas the F samples are considered fully dense.

In contrast, areas that were left unetched can be identified at the boundaries of the melt pools and within the melt pools themselves. Earlier research findings support the assertion that these zones correspond to the positive segregation of Cr and Mo. This segregation takes place during solidification due to the partitioning of these elements into the final liquid phase to solidify. This phenomenon is typically observed at cellular and dendritic boundaries, as well as at the interfaces of scan tracks and melt pools. Such localization contributes to the formation of retained austenite within AM maraging steels (Tonolini *et al.*, 2022).

Interestingly, despite Cr and Mo working as ferrite stabilizers, their increased concentration within the segregated regions has a localized impact. This leads to a reduction in the martensite starting temperature (Ms) of the steel to approximately -43 °C, as calculated using the empirical equation introduced by (Liu *et al.*, 2001). Consequently, austenite is stabilized at room temperature within these regions.

Finally, it is worth noting that the hardness of the F samples, measured at 54.6 ± 0.2 HRC, is approximately 1% higher than that of the AM samples, which measured 53.9 ± 0.2 HRC. This observation serves as evidence that the chosen heat treatment parameters were aptly tailored to their respective materials.

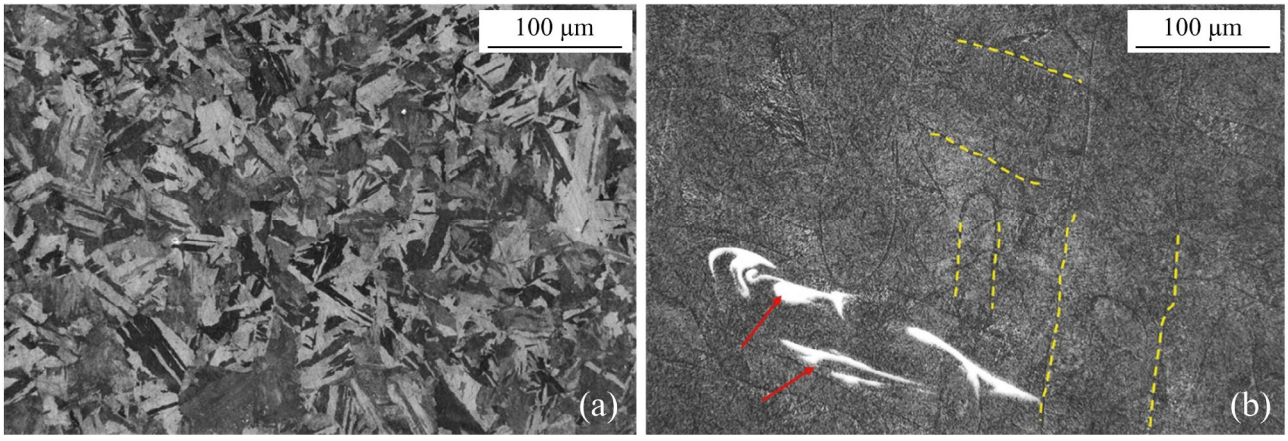

Fig. 1 – (a) Forged sample etched with Fry's reagent; (b) AMed sample etched with Nital 4%, the dashed yellow lines highlight some melt pool boundary, and the red arrows point at unetched zones that correspond to segregation of Cr and Mo.

The results from cavitation tests are represented in Fig. 2, illustrating MDE and MDER as a function of exposure time. These data represent the mean values obtained from two repetitions of the tests. In accordance with ASTM G32 standards, it is established that, the material accumulates plastic deformation and internal tensions before experiencing significant material loss (incubation period). This period corresponds to a time when the erosion rate is zero. Although the erosion rate values during the initial hours were not precisely zero, these were considered part of the incubation period due to the extremely low mass loss. This interpretation is further supported by the results of the analysis presented in Fig. 3, where the erosion rate is measured by plotting a linear regression in the steady-state period while the x-intercept of this linear regression is the incubation period (Taillon *et al.*, 2016). An incubation period of 4 hours and 7 hours was calculated for the AM and F alloys, respectively (Fig. 3). Furthermore, the analysis in Fig. 3 also reveals that, following the incubation period, the erosion rate for both materials remain nearly

constant, approximately at 0.67 mg/h in the steady-state erosion regime. After 24 hours of exposure, a total material loss of 13.5 ± 0.8 mg (MDE: 6.5 ± 0.4 μm) and 10.7 ± 2.9 mg (MDE: 5.2 ± 1.4 μm) is recorded for the AM and forged samples, respectively.

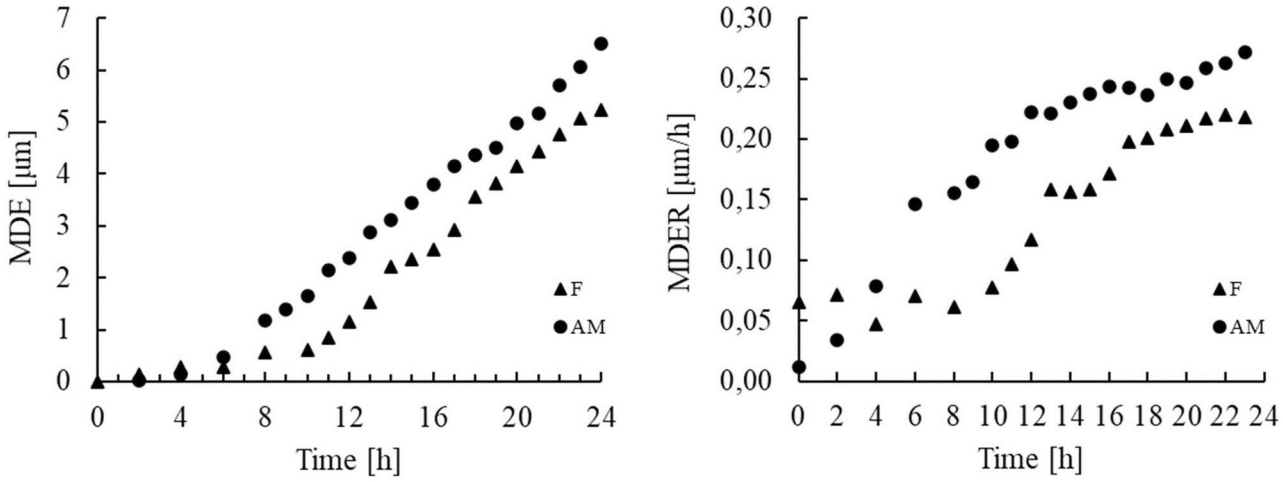

Fig. 2 – Mean Depth of Erosion (MDE) and Mean Depth of Erosion Rate (MDER) as functions of exposure time.

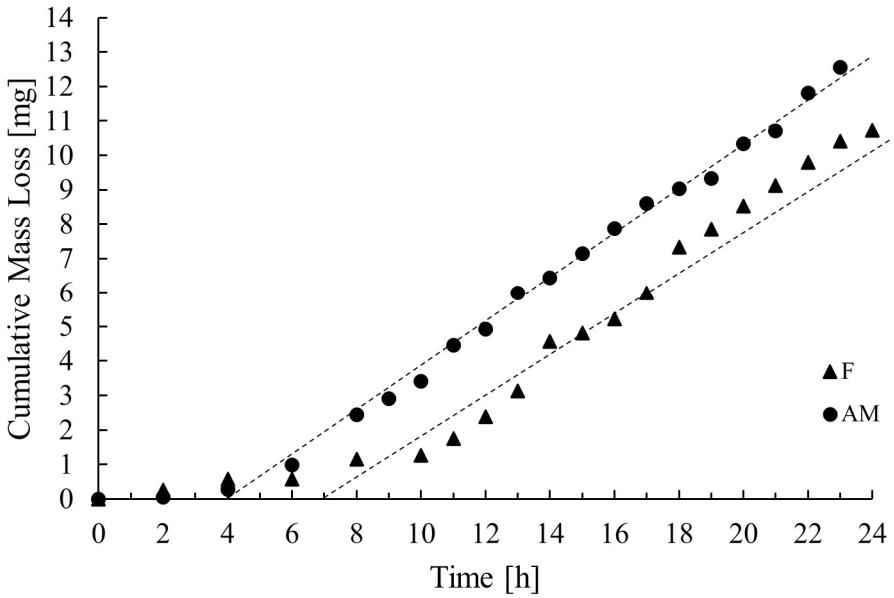

Fig. 3 – Cumulative mass loss as a function of exposure time.

In Fig. 4 images from digital microscope reveal qualitatively how the erosion evolves over the samples surface. Since the total mass loss of the samples is low, few difference can be detected looking at the surface hour by hour with a low magnification optical analysis. Thus, just the observation made at 4h and 20h are presented. At 4h the surfaces appear already covered with a ring-like shaped grey shade. In fact, even though almost no mass loss was measured at this time interval, the surfaces were plastically deformed by the cavitation micro-jets and shock waves.

On the other hand, at 20h the erosion process was fully developed. The erosion ring-like pattern is characteristic of the “stationary specimen method” (Chahine *et al.*, 2014; Astm, 2021).

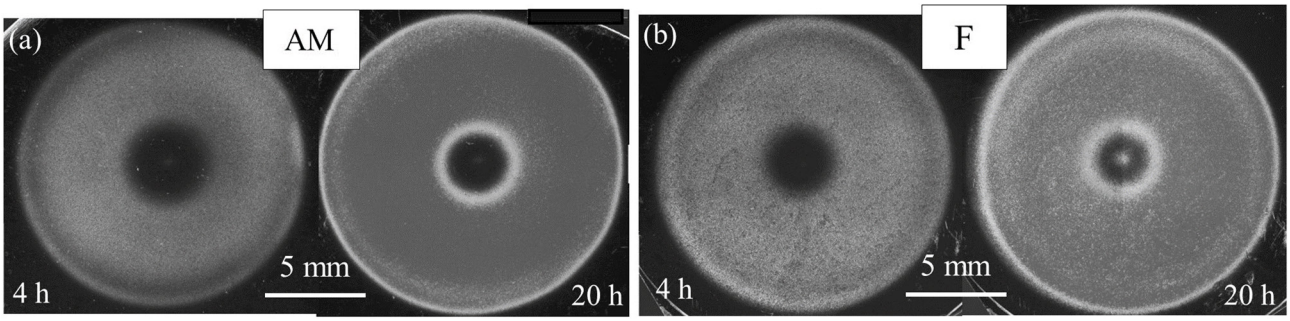

Fig. 4 – Stereomicroscopy images of (a) AM sample and (b) Forged sample after 4 and 20 hours of exposure to cavitation erosion.

The prior macroscopic observations provide limited insight into the underlying micro-damage mechanisms. However, upon conducting an optical microscopy analysis, the initial distinctions begin to emerge. Fig. 5 displays unetched sections of AM and forged samples at the end of the testing period. In the case of the AM sample, cracks propagate perpendicular to the surface, and rounded crates associated with porosity are visible. Conversely, in the forged sample, cracks propagate parallel to the surface, eventually removing larger debris. In detail, when the total stress reaches the maximum stress bearable by the material surface, a crack form. The crack keeps expanding and deforming, in a fatigue like manner, with continued exposure to the cavitation erosion conditions (Tian *et al.*, 2022).

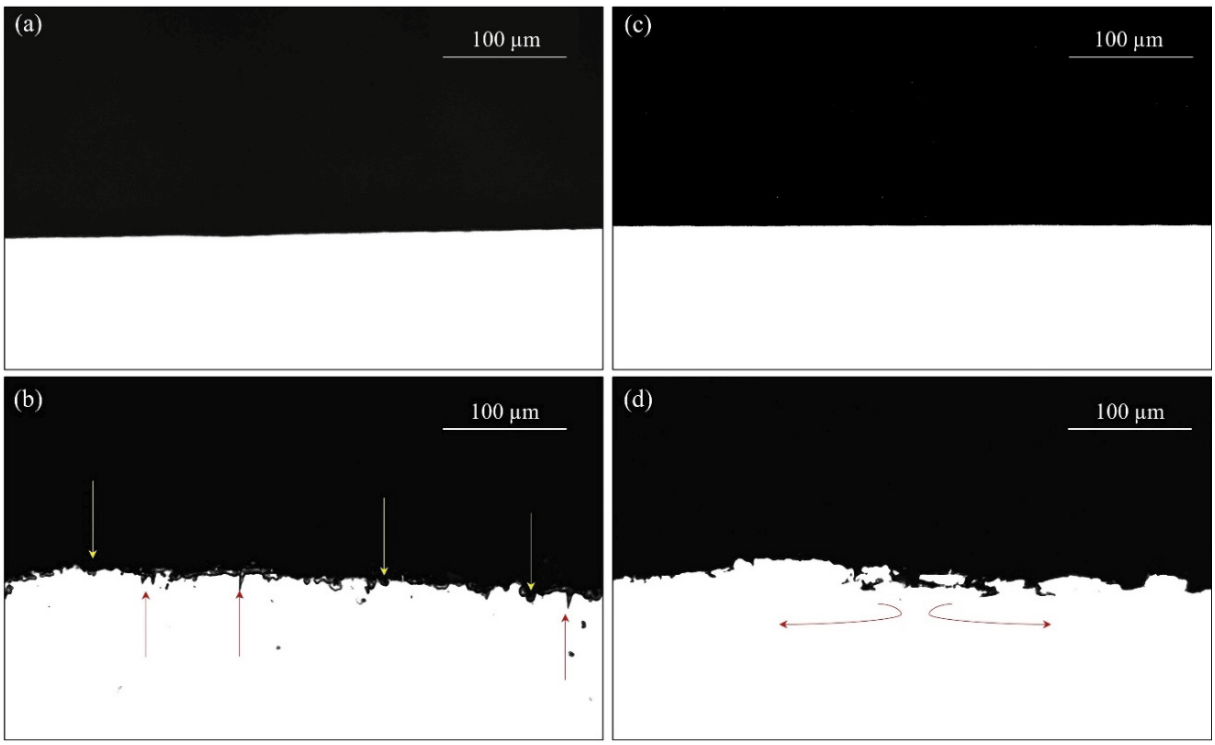

Fig. 5 - (a) AM sample surface before testing (b) AM sample surface at the conclusion of testing period, the yellow arrows point at rounded crates while the red ones at sharp cracks; (c) forged sample surface before testing; (d) forged sample surface at the conclusion of testing period, the red arrows indicate the direction of cracks propagation.

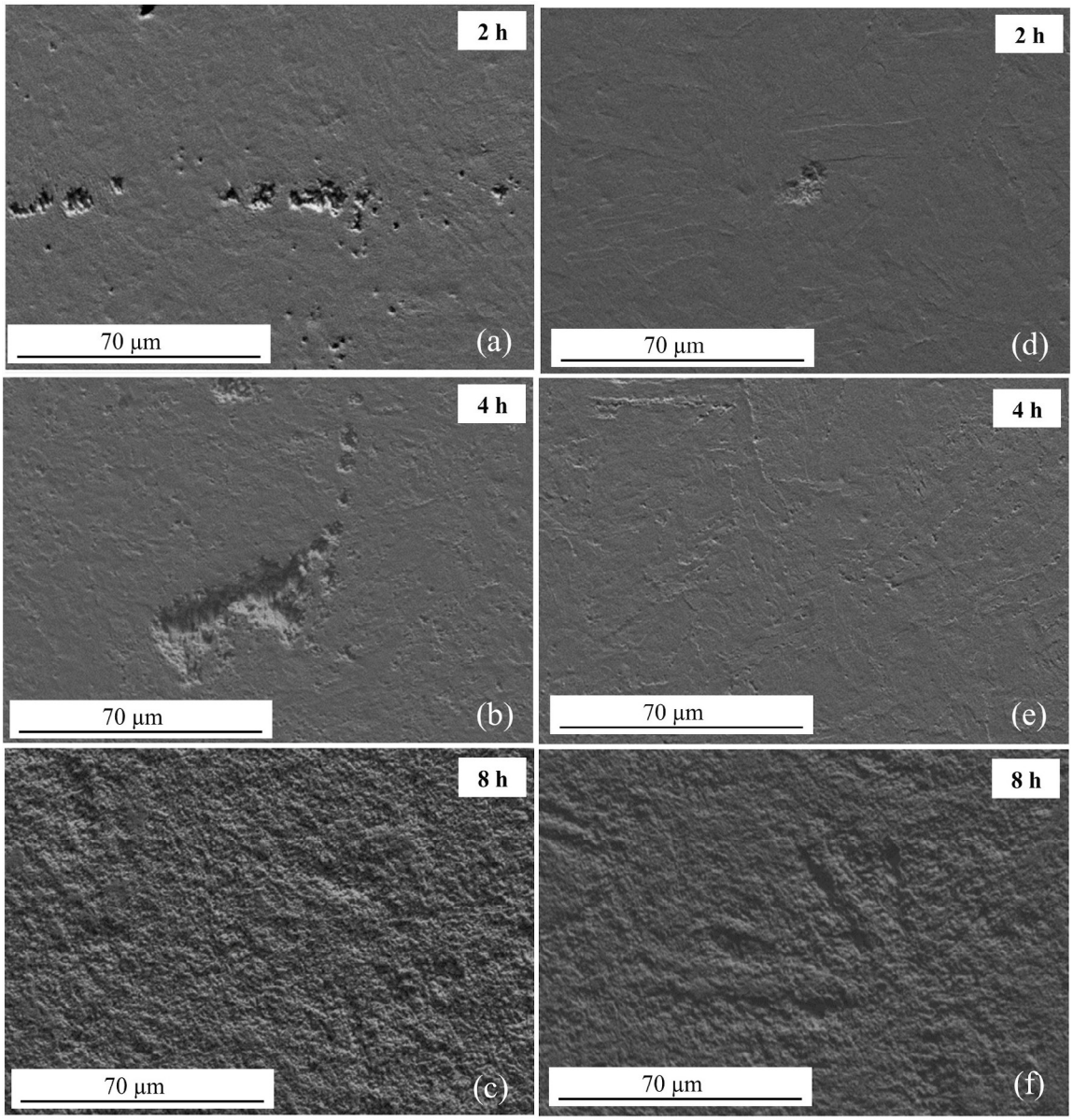

Fig. 6 – SEM images of the eroded surface at different testing times; (a-b-c) images of the AM sample; (d-e-h) images of the F sample.

At different testing intervals, SEM was employed to observe the morphology of the eroded surface. Following 2 hours of testing, several pits randomly emerged across the surface of both materials (Fig. 6a-d). Furthermore, the surface exhibited a progressively increasing roughness. These characteristics align with the typical early stages of cavitation erosion, marked by plastic deformation of the material rather than substantial mass loss (Heathcock *et al.*, 1982). The collapse of cavitation bubbles generates repetitive shock waves impacting the material's surface, inducing dislocation movements that result in plastic deformation and pitting, eventually leading to the removal of particles from the surface. Notably, the surface of the AM sample displayed a greater number of erosion initiation zones compared to the F sample.

At the 4-hour mark, corresponding to the incubation time of the AM samples, numerous larger and deeper craters emerged on the AM sample's surface (Fig. 6b). In contrast, as the forged sample had not yet reached its incubation

time, its surface remained predominantly covered with small erosion pits, uniformly distributed, and exhibited only minor corrugations (Fig. 6e). Few craters were found, similar to the observations from the previous step. The more evident damage for the AM sample is consistent with the shorter incubation periods as compared to the behaviour of F sample. Interestingly, several craters detected on the surface of AM sample followed preferential paths, consistent with some observations made at the 2-hour testing time.

the shape and spatial distribution of the craters identified on the surface of the AM sample during these initial stages of cavitation erosion therefore indicates that certain microstructural features serve as preferential sites for erosion nucleation, as known for the grain boundaries (Bregliozzi *et al.*, 2005).

In fact, microstructural analysis (Fig. 1) revealed that the melt pool boundaries persisted even after the aging treatment, and areas of elements segregation may contribute to the presence of austenite, even at room temperature. These can represent weak points where erosion cavitation damage can more easily nucleates. This can be supported by SEM analysis, which highlighted a linear pattern in the formation of erosion craters that could be influenced by the presence of the melt pool boundaries within the microstructure of the AM samples. Furthermore, after 4 hours of testing, a notable number of holes resembling the unetched segregations observed in the metallographic analysis became clearly visible. In addition, the effect of porosities, even if they are scarce, cannot be neglected as known from previous studies (Tocci *et al.*, 2019).

On the other hand, the more even distribution of smaller-sized craters in the microstructure of the F samples is consistent with their lower microstructural imperfections.

After 8 hours of exposure, the surface had undergone uniform erosion for both tested materials (Fig. 6c-f). This suggests that prolonged exposure to cavitation eventually led to a stress level that result in microcracks and subsequent material removal. Once this mechanism is developed, the surface appears uniformly eroded and the role played by microstructural imperfection on the initiation of the material removal mechanism cannot be recognised. This is supported by the fact that, after the incubation time, the erosion rate was the same for both materials.

4. Conclusion

This investigation has undertaken a comparative assessment of the resistance to cavitation erosion in 1.2709 maraging steel specimens produced via two distinct manufacturing methodologies: additive manufacturing and the traditional forging process. The empirical findings substantiate the capacity of additive manufacturing components to effectively contend with their forged counterparts, notwithstanding marked disparities in microstructural characteristics stemming from their different production techniques. Specifically, the additively manufactured components manifest a fully consolidated, fine-grained cellular martensitic structure, where the delineations of the melt pools and scan paths endure even post aging treatment. In contrast, the forged counterparts present a microstructure constituted by block of lath martensite. Notwithstanding these contrasting microstructural features, the outcomes of the cavitation erosion assessments manifest a remarkable similarity, implying that their respective hardness attributes, in fact equivalent, may be the determining factor of performance. In fact, the difference in material loss is statistically zero and the erosion rate in the steady-state erosion regime remain nearly constant, approximately at 0.67 mg/h for both materials, with the primary distinction being the shorter incubation time observed for the AM samples, which was 3 hours lower than that of the forged ones. Given the near-identical hardness of these parts, this phenomenon is likely attributed to microstructural features/defects at the surface that act as preferential sites for erosion nucleation, as indicated by a combination of optical microscopy and SEM analysis. Indeed, through SEM and metallographic analysis, it appears that microstructural imperfections, low-hardness austenite, melt pool boundaries and/or porosities may be responsible for the shorter incubation time of AM samples. Further research is essential to gain a deeper understanding of which specific defect clusters represent a greater risk for cavitation erosion. This understanding will enable the development for AM components with improved performance in the context of cavitation erosion resistance.

Acknowledgements

Financed by the European Union—NextGenerationEU (National Sustainable Mobility Center CN00000023, Italian Ministry of University and Research Decree n. 1033—17/06/2022, Spoke 11—Innovative Materials &

Lightweighting - CUP D83C22000690001). The opinions expressed are those of the authors only and should not be considered as representative of the European Union or the European Commission's official position. Neither the European Union nor the European Commission can be held responsible for them.

The authors would like to acknowledge MSc. Eng. A. Magistrelli of Bonomi Acciai for the preparation of the samples.

References

Abdullah, A.; Malaki, M.; Baghizadeh, E. On the impact of ultrasonic cavitation bubbles. Proceedings of the Institution of Mechanical Engineers, Part C: Journal of Mechanical Engineering Science, v. 226, n. 3, p. 681-694, 2012/03/01 2011.

ASTM. ASTM G32-16(2021) Standard Test Method for Cavitation Erosion Using Vibratory Apparatus 2021.

Bregliozzi, G. et al. Cavitation wear behaviour of austenitic stainless steels with different grain sizes. Wear, v. 258, n. 1, p. 503-510, 2005.

Brooks, H.; Brigden, K. Design of conformal cooling layers with self-supporting lattices for additively manufactured tooling. Additive Manufacturing, v. 11, p. 16-22, 2016.

Casati, R. et al. Aging Behaviour and Mechanical Performance of 18-Ni 300 Steel Processed by Selective Laser Melting. Metals. 6 2016.

Chahine, G. et al. Advanced Experimental and Numerical Techniques for Cavitation Erosion Prediction. 2014.

Girelli, L. et al. Investigation of cavitation erosion resistance of AlSi10Mg alloy for additive manufacturing. Wear, v. 402-403, p. 124-136, 2018.

Hattori, S. et al. Effect of liquid properties on cavitation erosion in liquid metals. Wear, v. 265, n. 11, p. 1649-1654, 2008.

Heathcock, C. J.; Protheroe, B. E.; Ball, A. Cavitation erosion of stainless steels. Wear, v. 81, n. 2, p. 311-327, 1982.

Liu, C. et al. A new empirical formula for the calculation of MS temperatures in pure iron and super-low carbon alloy steels. Journal of Materials Processing Technology, 2001, 1-3. p.556-562.

Peças, P. et al. Chapter 4 - Additive Manufacturing in Injection Molds—Life Cycle Engineering for Technology Selection. Advanced Applications in Manufacturing Enginering: Woodhead Publishing, 2019.

Piekło, J.; Garbacz-Klempka, A. Use of Maraging Steel 1.2709 for Implementing Parts of Pressure Mold Devices with Conformal Cooling System. Materials. 13 2020.

Taillon, G. et al. Cavitation erosion mechanisms in stainless steels and in composite metal-ceramic HVOF coatings. Wear, v. 364-365, p. 201-210, 2016.

Tian, Y. et al. In-situ SEM investigation on stress-induced microstructure evolution of austenitic stainless steels subjected to cavitation erosion and cavitation erosion-corrosion. Materials & Design, v. 213, p. 110314, 2022.

Tocci, M. et al. Wear and Cavitation Erosion Resistance of an AlMgSc Alloy Produced by DMLS. Metals. 9 2019.

Tonolini, P. et al. Wear and corrosion behavior of 18Ni-300 maraging steel produced by laser-based powder bed fusion and conventional route. Procedia Structural Integrity, 2022.

Venkatesh, G.; Ravi Kumar, Y.; Raghavendra, G. Comparison of Straight Line to Conformal Cooling Channel in Injection Molding. Materials Today: Proceedings, v. 4, n. 2, Part A, p. 1167-1173, 2017/01/01/ 2017.

Yang, Q.; Wu, X.; Qiu, X. Microstructural Characteristics of High-Pressure Die Casting with High Strength–Ductility Synergy Properties: A Review. Materials. 16 2023.